Exactly solvable chaos in an electromechanical oscillator

Benjamin A. M. Owens,[1,a)] Mark T. Stahl,[2] Ned J. Corron,[3] Jonathan N. Blakely,[3] and Lucas Illing[4]
[1]*Department of Mechanical Engineering and Materials Science, Duke University, Durham, North Carolina 27708, USA*
[2]*NASA, Marshall Space Flight Center, Alabama 35812, USA*
[3]*U.S. Army Research, Development and Engineering Command, Redstone Arsenal, Alabama 35898, USA*
[4]*Department of Physics, Reed College, Portland, Oregon 97202, USA*

(Received 3 May 2013; accepted 17 June 2013; published online 15 July 2013)

A novel electromechanical chaotic oscillator is described that admits an exact analytic solution. The oscillator is a hybrid dynamical system with governing equations that include a linear second order ordinary differential equation with negative damping and a discrete switching condition that controls the oscillatory fixed point. The system produces provably chaotic oscillations with a topological structure similar to either the Lorenz butterfly or Rössler's folded-band oscillator depending on the configuration. Exact solutions are written as a linear convolution of a fixed basis pulse and a sequence of discrete symbols. We find close agreement between the exact analytical solutions and the physical oscillations. Waveform return maps for both configurations show equivalence to either a shift map or tent map, proving the chaotic nature of the oscillations. [http://dx.doi.org/10.1063/1.4812723]

A common perception is that chaos is an unwieldy dynamical behavior that is best studied using numerical methods. In general, this view is correct. The vast majority of chaotic systems encountered in the fields of physics, biology, fluid dynamics, mechanics, and oceanography—to name a few—have no solutions that can be written out on paper in terms of known simple functions. Therefore, chaotic systems are typically viewed through the lens of numerical integration and characterized by estimates of their topological features and statistical properties. While valuable, these characterizations are complicated by the fact that the necessary numeric approximations lead to solutions that are at best shadowed by a true mathematical solution. This lends some uncertainty to results of numeric approaches. There is a class of chaotic systems, however, that penetrates this shroud of uncertainty, where exact solutions are known. Far from mathematical curiosities, such systems can be implemented in practice. As an example, we show in the current paper how an electromechanical experimental system, consisting of a magnetic mass on a spring that oscillates inside a coil that is used to sense and influence the magnet's motion, results in a hybrid system, whose chaotic oscillatory behavior can be described by an exact analytical solution.

I. INTRODUCTION

The exploration and characterization of chaos are well documented for low-dimensional systems. The complex dynamics of chaotic deterministic systems is generally characterized through numerical integration of the system equations, yielding estimates of the Lyapunov exponents, attractor topology, and fractal dimension.[1–3] Explorations of chaos exist in a vast array of fields including fluid dynamics,[1,4] cardiology,[5] neurology,[6,7] mechanics,[8,9] oceanography,[10] and communications.[11,12] Because of the nature of these systems, analytical solutions are commonly thought to be unobtainable.

However, exceptions exist. Exact analytical solutions have been developed for several dynamical systems showing chaotic behavior. Katsura and Fukuda laid out several examples of one-dimensional chaotic maps with exact solutions.[13] Umeno applied chaotic solvability to Belousov-Zhabotinski chemical reactions, matching analytic functions to experimental return maps.[14] Rollins and Hunt created a simple nonlinear circuit producing a one-dimensional, noninvertible map with a period doubling route to chaos that admits exact calculation.[15] Drake and Williams showed equivalent descriptions of common chaotic systems in the form of linear, time-invariant systems with random inputs, which produced outputs indistinguishable form those of the chaotic systems.[16] Corron explored chaotic ordinary differential equations possessing an exact symbolic dynamics.[17] More recently, Corron and Blakely showed a theoretical hybrid system with chaotic folded band topology and exact solvability.[18]

In the present paper, we report the construction and behavior of an electromechanical chaotic oscillator, which can be described by a model that admits exact analytic solutions. Following the example from theoretical and purely electrical systems,[14–19] this oscillator is a hybrid construction made up of analog and digital systems. Instead of voltage and current oscillations, however, chaotic oscillations of proof masses are considered.

The experimental system consists of a linear mechanical oscillator and a hybrid electrical system with analog and digital components. The mechanical oscillator is formed by two

a)benjamin.owens@duke.edu

connected magnetic proof masses attached to springs. Each proof mass oscillates within a wire coil allowing electromagnetic coupling between the mechanical and electrical part of the system. The primary coil is electrically driven to provide a negative damping effect, while the secondary coil exerts a constant force. The constant electromagnetic forcing is switched between two values based on the position and velocity of the system. The electrical system can be tuned to produce two types of chaotic oscillations; one with a topological structure similar to the Lorenz butterfly attractor[1] the other similar to a Rössler's folded-band.[2]

The mathematical model equations used to describe the system provide solutions that are both solvable and provably chaotic. These solutions can be written down in the form of a linear convolution of a symbol sequence and a fixed basis function. Given the discrete, measured symbols of the electromechanical system, an analytical solution for the system can be constructed that matches well with the observed system behavior. This match between theory and experiment proves the realizability of mechanical configurations of these types of systems and opens the door for further exploration into solvable chaotic systems.

The paper is organized as follows. Section II introduces the experimental system. Section III discusses the governing equations and the analytical solutions. Next, Sec. IV lays out results from experimental trials and compares the collected data to analytic solutions reproduced from the symbol sequences of the experimental results. Conclusions then follow in Sec. V.

II. ELECTROMECHANICAL OSCILLATOR

The electromechanical oscillator is a mechanical spring-mass system that is coupled to active electronic circuits. In this section, we first describe the mechanical configuration of the spring-mass system and derive a mathematical model for the mechanical oscillator. We then describe the design of two electromagnetic coils that couple the active electronic circuits to the mechanical system.

A. Mechanical oscillator

The full mechanical system and schematic are shown in Fig. 1. The frame for the system is constructed using steel strut channels and has a height of 1.75 m and a width of 1 m. This rigid frame holds a spring-mass system, which is assembled using two opposing spring sets and two separate masses connected by braided fiber fishing line. Each spring set comprises four parallel springs that are suspended from brackets at the top of the frame. Hanging from each spring configuration are three joined cylindrical neodymium magnets, which provide the mass for the mechanical oscillator. A pair of rod and bolt connectors are attached to both ends of the magnets and provide connection points for the fishing line as well as rigid support for the vertical orientation of the magnets. The hanging masses are connected to each other using a long line passing through low-friction pulleys at the bottom of the frame. This symmetric configuration was chosen to minimize the effects of gravity on the mechanical system.

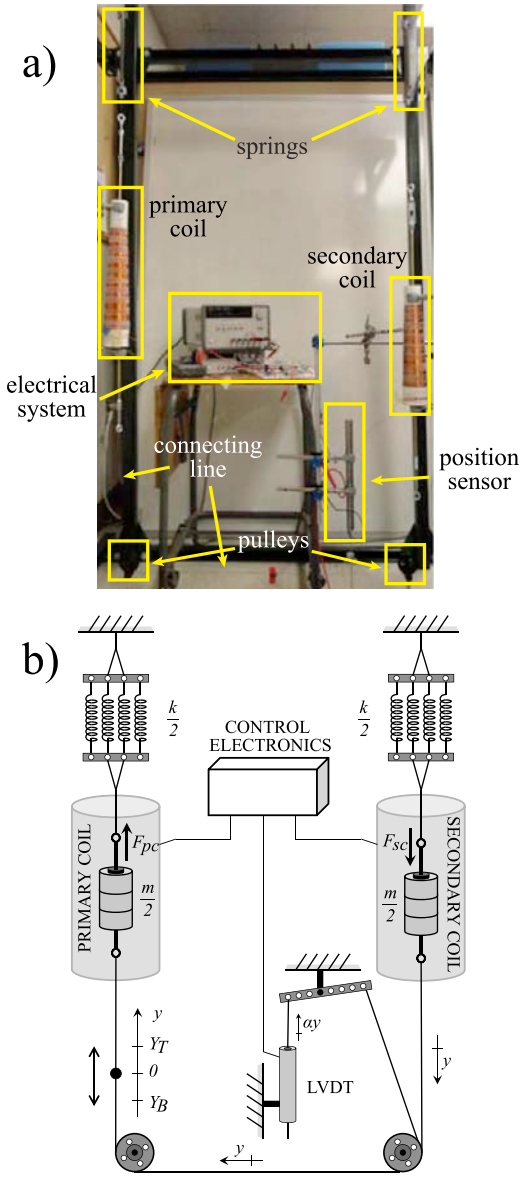

FIG. 1. (a) Labeled image and (b) schematic of a linear oscillator system with electrical and mechanical components and measuring equipment.

The complete line of the spring system down through the magnets and pulleys on one side and up through magnets and the springs on the other constitutes the primary axis of motion for the system, which we denote as y. To mitigate radial motion away from this axis, all the attaching lines between the various mechanical components are held under considerable tension. As seen in Fig. 1, each of the left and right segments of the axis of motion line pass through coils of magnetic wire wound about a section of PVC pipe. Each coil is controlled by electrical circuitry and coupled to the magnets by induced magnetic fields in the coils. In Fig. 1, the coil on the left is designated the primary coil, and its function is to induce a negative friction. The coil on the right is called the secondary coil and provides a switchable fixed point. It is the effect of the coils and the active electronics that yield the solvable chaotic dynamics.

The eight springs used in the system come from McMaster-Carr and have estimated individual constants of

19.2 N/m and an unstretched length of 6.35 cm. Under experimental line tensioning and no electromagnetic coil forcing, the static spring stretch is set to 17.1 cm, which is well below the maximum elastic deflection of 26.0 cm and within the linear range of motion for the springs. All six magnets are rare-earth permanent neodymium of type N52 from K&J Magnetics with a maximum residual flux density $B_r = 1.48$ T. Each magnet measures 2.54 cm in diameter, 1.27 cm in length, and 48.0 g in mass. With the rigid attaching pieces, the magnet systems on either side have a mass of ≈460 g for a combined system mass of ≈ 920 g.

B. System model

To derive the equations of motion, a couple of considerations are made to simplify the system. First, the pulleys are assumed to be massless and frictionless, allowing any nonconservative friction losses or inertial effects resulting from their motion to be ignored. Next, because the two sides are attached by a single line, the tension is assumed to be equal and constant throughout the line. This also means that the oscillations of the magnets on each side can be assumed to be equal along the primary axis and centered about a point set by the line tension and the weights of the respective sides of the system.

Each set of magnets, considered now as a single, long magnet, is cylindrical, uniformly magnetized in the vertical direction, and moves along the central axis of a coil, i.e., along the vertical axis of motion y. When a current I is applied to the coil, it generates a magnetic field $\mathbf{B}_{\text{coil}}$ that interacts with the magnet, resulting in a force $\mathbf{F}_{\text{mag}}$. Throughout, we assume that the current I varies slowly in time such that $\mathbf{B}_{\text{coil}}$ can be treated as a steady state field. Cylindrical symmetry of the coil's magnetic field together with the vertical alignment of the magnet implies that the resulting magnetic force is in the vertical direction,

$$\mathrm{F}_{\text{mag}} = F_{\text{mag}}\hat{y}. \tag{1}$$

Taking into account previous considerations, we can apply Newtonian mechanics to get the equation of motion

$$m\ddot{y} + c\dot{y} + ky = F_{\text{mag}}, \tag{2}$$

where F_{mag} is the effective magnetic force, k the effective spring constant of the system, and c the lumped viscous damping coefficient.

In this system, the magnetic force due to the primary coil F_{pc} is directly proportional to the velocity of the oscillating magnet and represents a *negative* viscous friction term, whereas the force due to the secondary coil F_{sc} represents an offset term that is switched between two constant values as a function of the magnet's position and velocity. The total magnetic force is therefore

$$F_{\text{mag}} = F_{\text{pc}} + F_{\text{sc}} = \frac{\nu^2}{R_N}\dot{y} + F_{\text{sc}}(y, \dot{y}), \tag{3}$$

where ν is a geometry dependent coefficient and R_N is the magnitude of the negative resistor, both detailed in Sec. II. Using Eq. (3), Eq. (2) can be written as

$$\ddot{y} - 2\zeta\omega_n\dot{y} + \omega_n^2(y - y_d(t)) = 0, \tag{4}$$

where the resonance frequency is $\omega_n^2 = k/m$, the effective damping ratio is $\zeta = (\nu^2/R_N - c)/(2m\omega_n)$ and $y_d(t)$ is a time-varying oscillation offset caused by F_{sc}. The time-varying offset y_d is modeled by a guard condition and is a function of the oscillator amplitude. It is

$$\dot{y} = 0 \Rightarrow y_d = Y_B + (Y_T - Y_B) \cdot H(y - Y_0), \tag{5}$$

where Y_B and Y_T are the bottom and top set points, Y_0 is a threshold, and the Heaviside function H is defined as

$$H(y - Y_0) = \begin{cases} 1 & \text{if } y \geq Y_0 \\ 0 & \text{if } y < Y_0. \end{cases} \tag{6}$$

The choice of the threshold Y_0 enables selection of the butterfly or folded-band oscillator. To obtain the butterfly topology, the threshold is the midpoint $Y_0 = (Y_T + Y_B)/2$. For the folded band, the threshold can be either set point $Y_0 = Y_{\text{T}}$ or $Y_0 = Y_B$. The guard condition is realized using a position sensor and control electronics that switch the fixed points by controlling the force F_{SC} due to the secondary coil. Additionally, the electronics controlling the primary coil can be tuned for different levels of negative damping on the moving masses. The design and implementation of the magnetic coils are described in the remainder of this section.

C. Coil design

The coils are made by winding a single continuous copper wire in many layers onto a PVC pipe, one-layer on top of the other and each layer shortened with respect to the previous one by starting it 2.54 cm further away from the coil's top end. With this winding, we approximate a coil for which the number of turns per unit length, $n(y)$, increases linearly with distance,

$$n(y) = c_n y, \quad y \in [0, L_c]. \tag{7}$$

Here, the origin of the coordinate system is at the top of the coil, the y-axis is pointing downward, L_{c} is the length of the coil, and $c_n = 2N_{\text{turns}}/L_c^2 \approx 16\ \text{cm}^{-2}$ is a constant.

To obtain an expression for the magnetic force, we model the coil, with its dense helical windings, as a continuum of current-carrying circular loops. By Newton's third law, the force of a single such loop on a magnet is identical in magnitude and opposite in direction to the force of the magnet on the loop. The force of the entire coil on the magnet, $\mathbf{F}_{\text{mag}}$, can therefore be obtained by summing the contributions from the force of the magnet on all loops,

$$\begin{aligned} \mathrm{F}_{\text{mag}} &= -\int \mathrm{J}_{\text{coil}} \times \mathrm{B}_{\text{mag}} d\mathrm{V} \\ &= \left(2\pi r_c I \int_0^{L_c} n(\bar{y})\, B_{\rho,mag}(r_c, \bar{y} - y) d\bar{y}\right)\hat{y}, \end{aligned} \tag{8}$$

where $\mathbf{J}_{\text{coil}}$ is the coil current density, I is the current in the coil's wire, r_{c} is the coil radius, and L_{c} is the coil length. $B_{\rho,mag}(r_{\text{c}}, \bar{y} - y)$ is the radial component of the magnet's

magnetic field expressed in cylindrical coordinates, while the magnet's geometric center is at position y. The force depends on the geometry of the coil through $n(\bar{y})$ and on the geometry of the magnet through $B_{\rho,\mathrm{mag}}$. These dependencies are lumped into a single function ν, which allows us to express the magnetic-force as

$$F_{\mathrm{mag}} = \nu(y)I. \tag{9}$$

In the limit where the permanent magnet can be approximated as a dipole magnet with dipole moment $\mu = \mu\hat{y}$ and the coil geometry is assumed to be described by Eq. (7), this function becomes

$$\nu(y) = \frac{\mu\mu_0 c_n}{2}\left(\frac{(L_c - y)^3 - y r_c^2}{\left(r_c^2 + (L_c - y)^2\right)^{3/2}} + \frac{y}{\sqrt{y^2 + r_c^2}}\right). \tag{10}$$

A simplified expression is obtained for the case of a long coil ($L_c \gg r_c$) and magnet positions away from the coil edges ($L_c > y \gg r_c$). In this case,

$$\nu(y) \approx \mu\mu_0 c_n. \tag{11}$$

Figure 2(a) depicts the dimensionless quantity $\nu(y)/(\mu\mu_0 c_n)$ for three cases. The (red) dashed line corresponds to Eq. (10). The (black) dashed-dotted line is the result of a numerical integration that uses Eq. (7) to model the coil and the exact expression for the magnetic field of a 3.81 cm long cylindrical magnet with a 2.54 cm diameter. The difference is due to the dipole approximation for the finite-size cylindrical magnet. In the limit where the size of the cylindrical magnet is decreased to zero, the prediction in Eq. (10) is recovered. The (blue) solid line is the numerical result for the case where the cylindrical magnet is considered and the physical coil is mimicked by summing over contributions from the discrete coil layers.

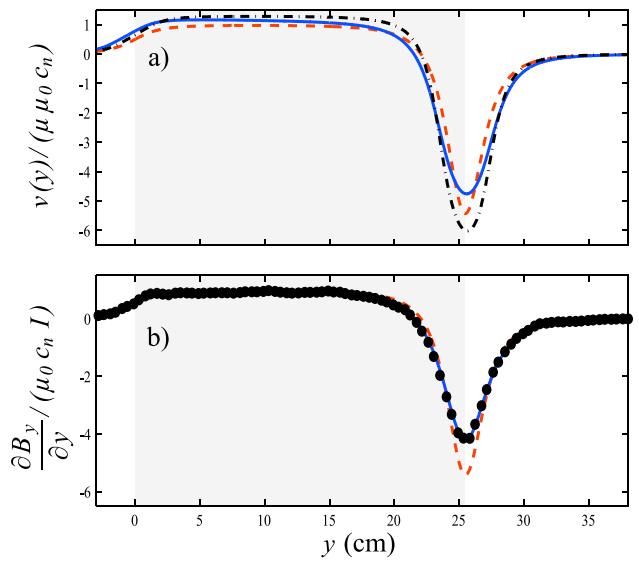

FIG. 2. (a) Normalized ν as a function of position: dashed line (red), dipole magnet, Eq. (10) assuming the dipole approximation; dashed-dotted line (black), numerical calculation using a cylindrical magnet; solid line (blue), cylindrical magnet and layered coil. The shaded region indicates the extent of the coil. (b) Normalized gradient of the coil's on-axis magnetic field: Circles (black), estimates from measured magnetic field data for the primary coil; dashed line (red), Eq. (10); solid line (blue), layered coil.

To characterize the coils, each was supplied with a constant current I, the resulting on-axis magnetic field was measured, and the normalized field gradient determined, as shown for the primary coil in Fig. 2(b) by (black) circles. Since the force on a vertically aligned dipole magnet is $\mathbf{F}_{\mathrm{mag}} = \mu\partial B_{\mathrm{coil}}/\partial y\,\hat{y}$, one finds that

$$\nu(y) = \frac{\mu}{I}\frac{\partial B^{\mathrm{coil}}}{\partial y}, \tag{12}$$

the normalized field gradient should correspond to $\nu(y)$, in the dipole approximation. As seen in Fig. 2(b), the measured result is indeed close to the theoretical prediction given by the dipole approximation in Eq. (10). A better match between data and theory is obtained when the layered structure of the coil is taken into account. The result of such a calculation is shown in Fig. 2(b) as a solid (blue) line.

As is evident from Fig. 2, $\nu(y)$ is constant, with $\nu = \mu\mu_0 c_n$, in a region extending from 3 to 20 cm, nearly two thirds the coil length. The chaotic oscillations of our magnets are entirely contained within this region. Therefore, by applying a constant direct current to the secondary coil, the constant offsetting force F_{sc} in Eq. (3) can be obtained.

D. Primary coil

The goal of the primary coil is to provide a physical realization of negative damping in the spring-mass system. To this end, the coil is connected to an active electronic circuit that provides a negative resistance to the electric potential induced by a magnet moving along the coil's axis. The negative resistance is the source of power that is required to sustain the mechanical oscillations in the system.

To implement the velocity dependent primary coil force F_{pc}, we utilize the emf ε that a moving magnet induces across the coil. Theoretically, the induced emf is obtained from Faraday's law by considering the change in time of the magnetic flux through a horizontal circular loop of radius r_c lying within the coil walls at position $\bar{y}$

$$\varepsilon = -\frac{d\Phi(\bar{y} - y)}{dt} = \frac{\partial\Phi(\bar{y} - y)}{\partial\bar{y}}\dot{y}, \tag{13}$$

where y denotes the position of the magnet. Since there are no magnetic monopoles, there is a zero total flux through the closed surface of a Gaussian pillbox formed by two such loops separated by an infinitesimal distance $d\bar{y}$. The difference $d\Phi$ between the magnetic flux through the top loop and the flux through the bottom loop is therefore exactly balanced by the flux through the sidewall of the pillbox. This implies that $\partial\Phi/\partial\bar{y} = -2\pi r_c B_{\rho,\mathrm{mag}}(r_c,\ \bar{y} - y)$. As there are $n(\bar{y})$ loops at position $\bar{y}$, the total emf across the coil is

$$\begin{aligned}\varepsilon &= -\left(2\pi r_c \int_0^{L_c} n(\bar{y})\, B_{\rho,\mathrm{mag}}(r_c, \bar{y} - y)\, d\bar{y}\right)\dot{y} \\ &= -\nu(y)\dot{y}.\end{aligned} \tag{14}$$

This emf ε is used to induce an opposing current in the coil via a negative resistance, implemented using an active electronic circuit.

A schematic of the negative resistance circuit used to drive the primary coil is shown in Figure 3. The dotted box represents the primary coil, and the elements within the box depict an equivalent electrical model for the actual physical coil. For the model, we directly measure the series resistance $R = 65\ \Omega$ and inductance $L = 220$ mH. The induced emf ε varies in proportion to the axial velocity of the magnet in the coil per Eq. (14). A LM675T power operational amplifier is used to drive the coil via the 33 Ω power feedback resistor. Two capacitors are included to suppress high-frequency oscillations. The remaining discrete components are designed to compensate for the coils internal impedance and provide a negative resistance. The 22 H inductor is realized by using active components in a general impedance converter (GIC) circuit.[20]

At low frequency, the circuit exhibits a negative resistance as desired. Neglecting the effects of the capacitors, analysis of the circuit reveals that the current in the coil is given by

$$i = -\frac{\varepsilon}{R_N}, \tag{15}$$

where the magnitude of the negative resistance is

$$R_N = \frac{R_G}{100} - R, \tag{16}$$

and R_G is an adjustable resistance implemented with trimmer potentiometers. In practice, decreasing R_G corresponds to increasing oscillator gain; however, stability of the feedback circuit requires $R_G > 100\,R$, and the negative resistor fails for R_G less than this threshold. Substitution of this current into Eq. (3) gives a velocity dependent force

$$F_{pc} = \frac{\nu^2}{R_N}\dot{y} \approx \frac{(\mu_0 \mu c_n)^2}{R_N}\dot{y}, \tag{17}$$

as desired.

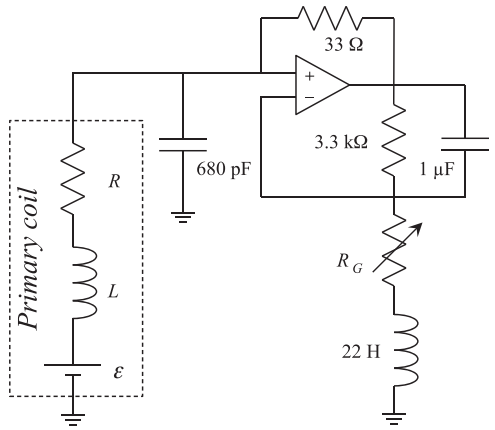

FIG. 3. Negative resistance circuit used for driving the primary coil. Elements in the dashed box model the circuit characteristics of the primary coil with $R = 65\ \Omega$ and $L = 220$ mH.

E. Secondary coil

The function of the secondary coil is to shift the oscillator's fixed point between two levels depending on the guard conditions from Eqs. (5) and (6) and the threshold definitions. The shift is provided by inducing a constant force on the secondary magnet in the spring-mass system using a constant current through the secondary coil.

Figure 4 shows a schematic of the electronic circuit used to implement the guard condition and drive the current in the secondary coil. To detect the position and velocity of the mechanical system, a commercially available linear variable differential transformer (LVDT) position sensor (Measurement Specialties DC-EC 2000) is used. The output voltage $\nu(t)$ from the position sensor drives two comparators that detect the logical conditions $\nu > V_0$ and $\frac{d\nu}{dt} < 0$, where V_0 is an adjustable threshold that enables tuning between shift and folded band dynamics. A low-pass filter (LPF) is used to suppress any fast electrical oscillations due to switch bounce or noise in the mechanical sensor. A digital latch comprising discrete AND and OR gates realizes the logical output of the guard condition, which determines the polarity of a signal applied to the secondary coil.

The secondary coil is driven by a power operational amplifier (LM675T) configured as a comparator to distinguish logic levels. The amplifier is powered with ± 15 V, and its output supplies the coil with -13.6 V and 13.2 V for $s(t) = 0$ and 1, respectively. The series resistance of the secondary coil is 40 Ω, implying a 670 mA change in the direct current at a transition in the logic state.

To change the particular configuration of the system, the only parameter varied is V_0. When V_0 is set to a voltage in the middle of voltages for the upper and lower oscillation centers, the system will show shift dynamics. This center threshold V_0 represents the physical Y_0 value of Eq. (5).

III. SIMPLIFIED SYSTEM EQUATIONS

In order to analyze the electromechanical system, including guard conditions, governed by Eqs. (4)–(6), it is convenient to use a dimensionless model obtained by using the following substitutions:

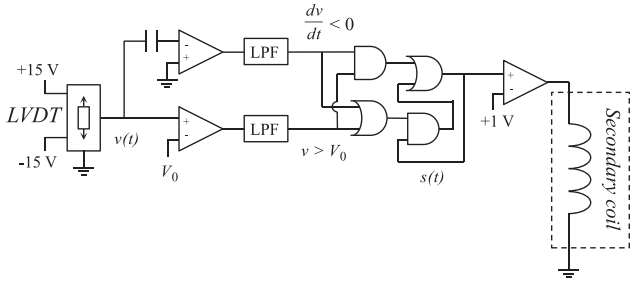

FIG. 4. Position sensor and logic circuitry used to implement guard condition and discrete switching with the secondary coil. The LVDT position sensor outputs a voltage that varies linearly with the displacement of the spring-mass system, and V_0 is an adjustable threshold used to select the butterfly or folded-band oscillations.

$$\tau = \frac{t}{T}, \quad u = \frac{y - C_2}{C_1}, \quad \text{and} \quad s = \frac{y_d - C_2}{C_1}, \quad \text{with period}$$
$$T = \frac{2\pi}{\omega_n \sqrt{1-\zeta^2}}. \tag{18}$$

With these substitutions, Eq. (4) simplifies to the dimensionless form

$$\ddot{u} - 2\beta\dot{u} + (\omega^2 + \beta^2)(u - s) = 0, \tag{19}$$

where $\omega = 2\pi$ is the oscillation frequency, $\beta = 2\pi\zeta/\sqrt{1-\zeta^2}$ is a positive coefficient that quantifies the degree of negative damping, and s is the discrete switching point state. Parameters C_1 and C_2 are dependent on the system being modeled. For the butterfly oscillator, $C_1 = (Y_T - Y_B)/2$ and $C_2 = (Y_T + Y_B)/2$. For the folded band, $C_1 = Y_T - Y_B$ and $C_2 = Y_B$. With these substitutions, s is a system dependent variable governed by a guard condition and state characterization of either

$$\dot{u} = 0 \Rightarrow s = \text{sgn}(u) \tag{20}$$

or

$$\dot{u} = 0 \Rightarrow s = H(u - 1) \tag{21}$$

for the Lorenz-butterfly or Rössler folded band topologies, respectively. Note, these equations follow the form found in Refs.17 and 19 and can therefore be similarly solved. Significantly, exact analytical solutions to both hybrid system configurations can be found.

A. Butterfly

It has been shown previously that Eq. (19) with guard condition (20) can be analytically solved.[17,19] Without loss of generality, we consider an initial condition coinciding with a triggered guard condition, $\dot{u} = 0$, such that $|u| \leq 1$. As such, the solution can be written as a linear convolution

$$u(t) = \sum_{n=0}^{\infty} s_n \cdot P(t - n), \tag{22}$$

$$\text{and} \quad s(t) = \sum_{n=0}^{\infty} s_n \cdot \phi(t - n), \tag{23}$$

where s_n is a weighting factor. The basis functions are shown in Fig. 5(a) and defined as

$$P(t) = \begin{cases} (1 - e^{-\beta})e^{\beta t} q(t), & t < 0 \\ 1 - e^{\beta(t-1)} q(t), & 0 \leq t < 1 \\ 0, & t \geq 1, \end{cases} \tag{24}$$

with

$$q(t)\cos\omega t - \frac{\beta}{\omega}\sin\omega t, \tag{25}$$

and

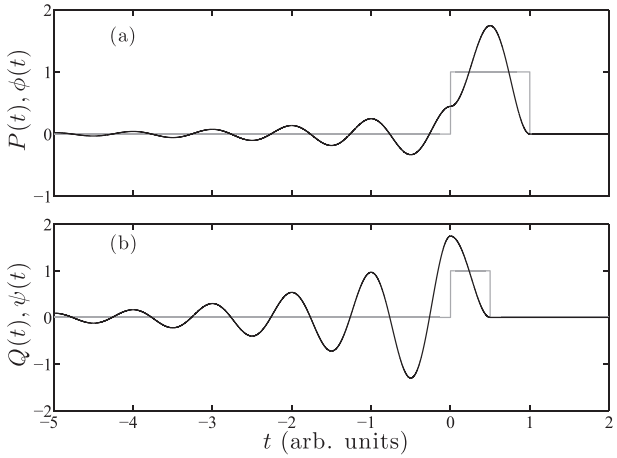

FIG. 5. Basis pulses for the solvable butterfly (a) and folded-band (b) oscillators.

$$\phi(t) = \begin{cases} 1, & 0 \leq t < 1 \\ 0, & \text{otherwise}. \end{cases} \tag{26}$$

Note here that it is assumed that the solution satisfies guard conditions at $t = n$ and $n + 1/2$ such that $\text{sgn}(u(n)) = \text{sgn}(u(n + 1/2))$ for all integer n. The weighting factors s_n are given as a sequence of binary symbols ± 1 corresponding to the switching state at each integer guard condition or $s_n = \text{sgn}(u(n))$. This definition means that switching transitions occur only at integer dimensionless time n.

In addition to the exact solution, it is useful to consider a return map. This map is a stroboscopic sampling of u for successive returns at integer times, yielding,

$$u_{n+1} = e^{\beta}(u_n - s_n) + s_n, \tag{27}$$

where $u_{n+1} = u(n+1)$ and $u_n = u(n)$. This recursion relation corresponds to a shift map with slope e^{β} for all $\beta > 0$. This map is closed on the interval $|u_n| < 1$ and for negative damping $0 < \beta < \ln 2$. A typical map is shown in Figure 6. Since this iterated map is piecewise linear with constant slope > 1, the map is necessarily chaotic, indicating that the hybrid system is likewise chaotic, having a corresponding Lyapunov exponent $\lambda = \beta$. This configuration has topological

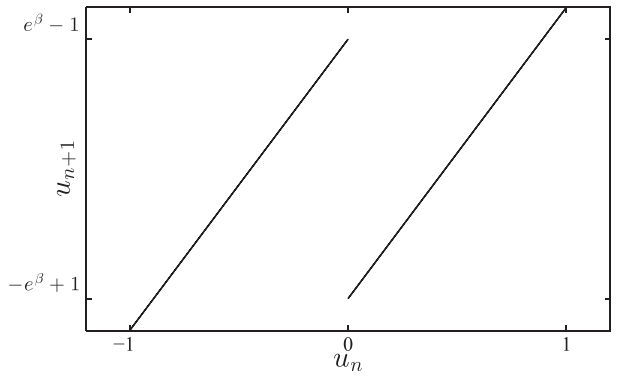

FIG. 6. Theoretical return map for the solvable oscillator exhibiting a butterfly attractor.

characteristics similar to that of the famous Lorenz attractor as will be shown graphically in the experimental and analytical comparisons in Sec. IV.

B. Folded band

Solutions can be similarly derived for the switching definition given by Eq. (21). Again we consider an initial condition coinciding with a triggered guard condition. Under this assumption, the solution states can be written as linear convolutions of weighted basis functions

$$u(t) = \sum_{m=0}^{\infty} \sigma_m \cdot Q\left(t - \frac{m}{2}\right), \tag{28}$$

$$s(t) = \sum_{m=0}^{\infty} \sigma_m \cdot \psi\left(t - \frac{m}{2}\right), \tag{29}$$

where σ_m is a weighting factor. The basis functions are shown in Fig. 5(b) and defined as

$$Q(t) = \begin{cases} (1 + e^{-\beta/2})e^{\beta t}q(t), & t < 0 \\ 1 + e^{\beta(t-1/2)}q(t), & 0 \le t < \frac{1}{2} \\ 0, & t \ge \frac{1}{2}, \end{cases} \tag{30}$$

with

$$\psi(t) = \begin{cases} 1, & 0 \le t < \frac{1}{2} \\ 0, & t < 0 \quad \text{or} \quad t \ge \frac{1}{2}. \end{cases} \tag{31}$$

In this case, the weighting factors σ_m are set to the discrete state of $s(t)$ for $m/2 \le t < m + 1/2$, and it follows that they are restricted to the set$\{0,1\}$. This solution is not valid for all possible oscillations of u but is limited to initial conditions bounded by

$$|u(0)| \le \frac{1 + e^{-\beta/2}}{1 - e^{-\beta/2}}, \tag{32}$$

which corresponds to small initial displacements of the physical system.

For the folded-band system, the return map used to help understand the system is based on successive maxima, instead of returns at integer times. For some arbitrary initial condition bounded by Eq. (32), a successive maxima return map is given by

$$u_{n+1} = \begin{cases} e^{\beta}u_n, & 0 < u_n \le 1, \\ -e^{3\beta/2}u_n + e^{\beta} + e^{3\beta/2}, & 1 < u_n < 1 + e^{\beta/2} \\ e^{\beta}u_n - e^{\beta} - e^{\beta/2}, & u_n > 1 + e^{-\beta/2}, \end{cases} \tag{33}$$

where u_n is the initial local maxima and u_{n+1} is the next maxima. This map is shown as three piecewise linear segments (a), (b), and(c), as seen in Fig. 7. Note that unlike the previous case, the return times are dependent on the system state, yielding

$$\Delta t = t_{n+1} - t_n = \begin{cases} 1, & 0 < u_n \le 1, \\ \frac{3}{2}, & 1 < u_n < 1 + e^{-\beta/2}, \\ 1, & u_n > 1 + e^{-\beta/2}. \end{cases} \tag{34}$$

The return time difference for $1 < u_n < 1 + e^{-\beta/2}$ is due to the folding mechanism as the system oscillates about a separate fixed point for an additional half cycle.

The properties of the return map (33), and hence the dynamics of the mechanical oscillator, depend on the particular value of the negative damping.[18] For small negative damping such that $\beta < \beta_1$, where

$$e^{\beta} \le 1 + e^{-\beta/2}, \quad \beta_1 \approx 0.8 \cdot \ln 2, \tag{35}$$

the iterated map is restricted to linear segments (a) and (b) in Fig. 7. In this case, the oscillator exhibits a folded-band topology similar to Rössler's simply folded band.[2] For $\beta_1 < \beta < \beta_2$ where

$$e^{\beta_2} = 2 + e^{-\beta_2/2}, \quad \beta_2 \approx 1.39 \cdot \ln 2, \tag{36}$$

the iterated map is bounded and visits segments (a), (b), and (c). In this case, the oscillator exhibits a second fold in its dynamics. In either case, the slope of the iterated map (33) is everywhere greater than one, so the bounded oscillations are necessarily chaotic. For $\beta > \beta_2$, the map is not closed and oscillations are unbounded.

IV. RESULTS AND DISCUSSION

The hybrid dynamical system was tuned with two configurations, producing two distinct experimental trajectories coinciding with those in the theoretical analysis above. Each analysis examines a large, continuous time data set to produce time-delay embedded phase projections and return maps corresponding to Figs. 6 and 7. Additionally, a smaller subset of these data sets were used to find a sequence of symbols for the discrete data. The symbols were then used to recreate an analytical waveform in dimensionless time, scaled, and compared to the physical experimental results.

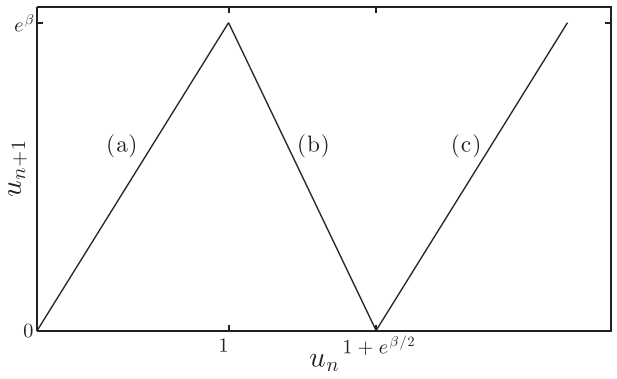

FIG. 7. Theoretical successive-maxima return map for the solvable folded-band oscillator.

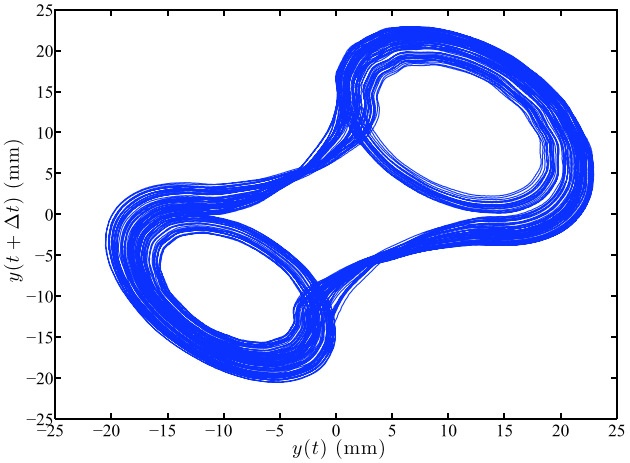

FIG. 8. Time-delay embedding ($\Delta t \approx 0.15\,T$) of the position data for the first system configuration to illustrate the butterfly attractor topology.

Position measurements were obtained using the LVDT position sensor, which was sampled using a data acquisition system. Remote placement of the position sensor was facilitated using a second string under tension and a mechanical linkage, which preserved a linear scaling of the true position for small displacements typical of the observed oscillations (see Fig. 1). The sub-Hertz oscillation data were significantly oversampled using 100 Hz digital sampling rates.

A. Butterfly

In the first configuration, the voltage V_0 and the resistance R_G were tuned to obtain chaotic oscillations exhibiting the Lorenz butterfly dynamics. A 5-min record of the position of the spring-mass system as well as the electronic switching state were captured and stored. Figure 8 shows the attractor obtained from this measurement using time-delay embedding ($\Delta t \approx 0.15\,T$) of the position data. A typical segment showing the continuous and switching states is shown in Figure 9. From the data, we estimate the period for the underlying harmonic oscillator at $T \approx 0.46$ s.

Figure 10 shows a return map constructed using position data sampled at guard conditions corresponding to possible switching events. We note that this return map shows a shift dynamic consistent with the desired butterfly topology.[19] From the average slope of each segment of the return map, we estimate the negative damping parameter to be $\beta = 0.47$.

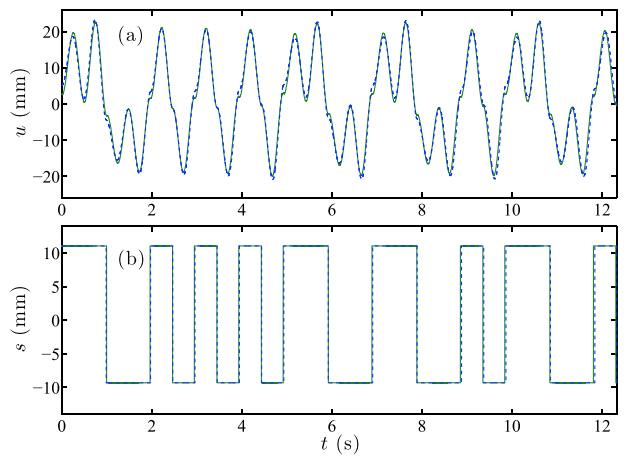

FIG. 9. A typical segment of experimental data and analytic solution for the oscillator exhibiting a butterfly attractor. Solid line (green) is the measured waveform, dashed (blue) is the analytical solution derived from the experimental symbol sequence.

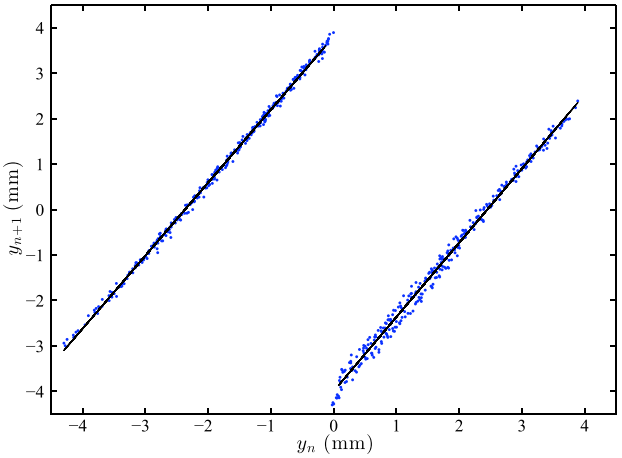

FIG. 10. Experimental return map (blue) for the oscillator exhibiting a butterfly attractor and with least squares fit slope lines (black) for each segment.

To show the analytically solvable nature of the mechanical oscillator, we overlay the corresponding analytic solution in dimensional form in Figure 9. For this solution, we estimate the parameters $Y_T = 11.03$ mm and $Y_B = -9.31$ mm. For the segment of measured waveform, the corresponding symbol sequence is read from the measured switching state. The analytic solution (22) and (23) is calculated from this symbol sequence and shown in the plots as dashed curves. A strong correlation between measured and analytic waveforms indicates that the mechanical system is reasonably well modeled by the exactly solvable chaotic oscillator exhibiting the butterfly topology.

B. Folded-band

In the second configuration, system parameters were tuned to obtain chaotic oscillations exhibiting folded-band dynamics. As with the first configuration, an extended time series of position and switching state was collected. Figure 11 shows the attractor obtained from this data with the same

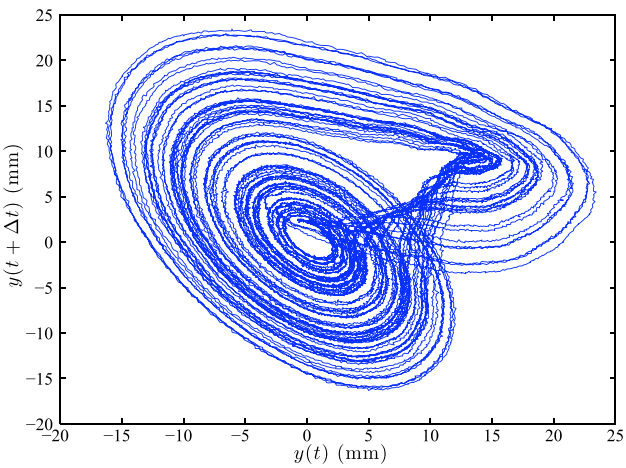

FIG. 11. Time-delay embedding ($\Delta t \approx 0.15\,T$) of the position data for the second system configuration to illustrate the folded-band topology.

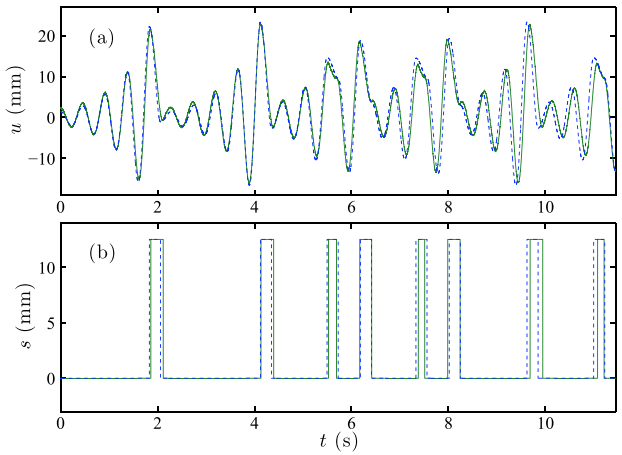

FIG. 12. A typical segment of experimental data and analytic solution for the folded-band oscillator. Solid line (green) is the measured waveform, dashed (blue) is the analytical solution derived from the experimental symbol sequence.

time-delay embedding as the first configuration. Figure 12 shows a typical segment of the two waveforms. The estimated period from the harmonic oscillations is unchanged from the first configuration, $T \approx 0.46$ s.

Figure 13 shows an iterate map with position data sampled at the successive local maxima of the response. This map shows a piecewise tent consistent with folded-band topologies.[18] The corresponding lines represent a least squares fit for the subsets of data that comprise each segment. Estimated β values from the three segments are $1.04 \cdot \ln 2$, $0.93 \cdot \ln 2$, and $0.2771 \cdot \ln 2$, respectively. The large error in the furthest right segment is a result of its short length and the somewhat arbitrary act of where to cut data segments, especially in noisy regions of the data.

As with the first configuration, we overlay the corresponding analytic solution in dimensional form in Figure 12 for the second configuration. For this solution, tuning parameters are adjusted such that $Y_T = 12.53$ mm and $Y_B = 0$ mm, with $\beta = 0.72$ estimated from the first branch of the return map. The analytic solution (28) and (29) is calculated from

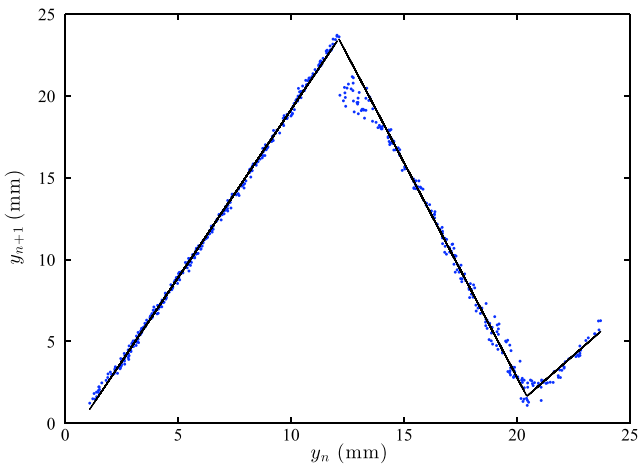

FIG. 13. Experimental successive-maxima return map (blue) for the folded-band oscillator with leastsquares best fit slope lines (black).

the corresponding symbol sequence read from the measured switching state. This is shown in the plots as dashed curves. Again, a strong correlation is apparent between the measured and analytic waveforms, indicating that the system is well modeled by the exact folded-band solutions.

Discrepancies between the two waveforms are largely a function of phase slip errors. Oscillations that just cross the guard condition threshold have a necessarily small amplitude for oscillation about that upper set point. This lends them a larger sensitivity to timing errors inherent in the system. These errors are to some extent a function of the electromagnetic switching event itself which induces a considerable, instantaneous torque and a considerable lateral force if the magnet is at all radially displaced from the axis of motion.

V. CONCLUSIONS

In this article, we detail the construction and testing of an experimental dynamical system that shows exactly solvable chaotic oscillations. Detailed theoretically in previous articles and replicated in electric systems, this system is an equivalent mechanical *and* electrical manifestation. With the execution of negative damping through the electromagnetic coupling between the magnet and coil and a simple switching condition, a chaotic oscillator is realized. Additionally, these oscillations can be represented as a linear convolution of basis functions. Figures show a clear tent map and dynamic shift map that indicate the chaotic nature of the oscillating system. While the approximations are less accurate than the electrical equivalents in the literature, symbol dynamics can be used to replicate the waveform with considerable agreement. This match between theory and experiment proves the realizability of mechanical configurations of these types of systems and opens the door for further exploration into solvable chaotic systems.

[1]E. N. Lorenz, J. Atmos. Sci. **20**, 130 (1963).
[2]O. Rössler, Phys. Lett. A **57**, 397 (1976).
[3]P. Holmes, Philos. Trans. R. Soc. London, Ser. A **292**, 419 (1979).
[4]R. W. Walden, P. Kolodner, A. Passner, and C. M. Surko, Phys. Rev. Lett. **55**, 496 (1985).
[5]L. Glass, A. L. Goldberger, M. Courtemanche, and A. Shrier, Philos. Trans. R. Soc. London, Ser. A **413**, 9 (1987).
[6]H. Sompolinsky, A. Crisanti, and H. J. Sommers, Phys. Rev. Lett. **61**, 259 (1988).
[7]A. Babloyantz and A. Destexhe, Proc. Natl. Acad. Sci. U.S.A. **83**, 3513 (1986).
[8]M. V. Berry, Eur. J. Phys. **2**, 91 (1981).
[9]R. Everson, Physica D **19**, 355 (1986).
[10]E. Tziperman, L. Stone, M. A. Cane, and H. Jarosh, Science **264**, 72 (1994).
[11]N. Corron and D. Hahs, IEEE Trans. Circuits Syst., I: Fundam. Theory Appl. **44**, 373 (1997).
[12]S. Hayes, C. Grebogi, and E. Ott, Phys. Rev. Lett. **70**, 3031 (1993).
[13]S. Katsura and W. Fukuda, Physica A **130**, 597 (1985).
[14]K. Umeno, Phys. Rev. E **55**, 5280 (1997).
[15]R. W. Rollins and E. R. Hunt, Phys. Rev. Lett. **49**, 1295 (1982).
[16]D. Drake and D. Williams, IEEE Trans Signal Process. **55**, 1379 (2007).
[17]N. J. Corron, Dyn. Contin. Discrete Impulsive Syst.: Ser. A-Math. Anal. **16**, 777 (2009).
[18]N. J. Corron and J. N. Blakely, Chaos **22**, 023113 (2012).
[19]N. J. Corron, J. N. Blakely, and M. T. Stahl, Chaos **20**, 023123 (2010).
[20]*Linear Circuit Design Handbook*, edited by H. Zumbahlen (Elsevier/Newnes Press, 2008).